EXPERIMENTAL STUDIES OF THE THERMODYNAMIC FIELDS OF A SUBSONIC COMPRESSIBLE SHEAR LAYER

Carson M. Kipp
Dept. of Aerospace and Mech. Engineering
University of Notre Dame
Notre Dame, Indiana, 46556, USA
ckipp@nd.edu

R. Mark Rennie
Dept. of Aerospace and Mech. Engineering
University of Notre Dame
Notre Dame, Indiana, 46556, USA
rrennie@nd.edu

Stanislav Gordeyev
Dept. of Aerospace and Mech. Engineering
University of Notre Dame
Notre Dame, Indiana, 46556, USA
sgordeye@nd.edu

Abstract

In this study, we report the static pressure, static and stagnation temperature, and inferred density of a subsonic compressible shear layer in order to gain insight into its underlying thermo-fluidic mechanism. Pressure measurements were obtained using a wall-mounted array of unsteady pressure sensors, while temperature measurements were derived from calibrated, low-pass corrected cold-wire Constant current Anemometry signals. The experimental procedure for the cold-wire calibration and the associated transfer function calculation, used to properly measure the static temperature, is discussed alongside the operating principle and the dynamic response of the cold-wire. Density measurements were inferred from off-axis digital holographic wavefront measurements, providing an estimate of the spanwise path integrated density perturbations through the shear layer. The shear layer was excited at the frequency and subharmonic of its most unstable mode to enhance spanwise uniformity and enable phase averaged measurements by controlling the vortex formation and pairing. Consistent with the complementary computational studies presented in DeFoor *et al.* (2026), the present results support the proposed thermo-fluidic mechanism of a subsonic compressible shear layer.

INTRODUCTION

The experimental investigation of the subsonic compressible shear layer remains an active area of research, particularly within the context of airborne optical systems, owing to the shear layer's highly variable density and hence index of refraction fields. Accurately predicting the thermodynamic and density fields of the shear layer, along with the physical mechanisms that produce them, therefore directly constrains the performance of such systems (Gordeyev *et al.* (2023)).

Previous studies have suggested that, for subsonic compressible (or weakly compressible) shear layers, compressibility does not strongly affect the development of the underlying velocity field, which is dominated by large scale vortical structures. Instead, the influence of compressibility manifests primarily in the thermodynamic field (Fitzgerald & Jumper (2004)). Building on this assumption, researchers have simulated the velocity field using an incompressible discrete vortex method with high fidelity, and subsequently recovered the associated pressure, temperature, and density spatial distributions through a thermodynamic model. The resulting "Weakly Compressible Model" (WCM) was found to correctly predict optical distortions, and was therefore assumed to capture the relevant mechanisms of the shear layer's density field.

However, more detailed studies revealed discrepancies in the magnitude of the predicted density gradients, particularly along the slip lines between vortical structures, when compared with computational fluid dynamics (CFD) simulations (Visbal (2009); Rennie *et al.* (2008)). In response, complementary two-dimensional CFD simulations and experimental studies were carried out to address this discrepancy, providing strong evidence for the existence of sharp density gradients in weakly compressible shear layers (Kipp *et al.* (2025); Oliva *et al.* (2025); DeFoor *et al.* (2026)). In particular, CFD simulations identified the stagnation temperature field as the source of these gradients, while the WCM does not predict such sharp stagnation temperature or density gradients. Moreover, Fitzgerald & Jumper (2004) argued that, since spatial changes in the stagnation temperature are due primarily to temporal changes in the pressure field,

$$\rho C_p \frac{DT_0}{Dt} = \frac{\partial P}{\partial t}, \tag{1}$$

and that the pressure field is smooth, sharp temperature gradients should not appear in shear layers. However, the conclusions presented in Oliva *et al.* (2025) suggest that this discrepancy arises because the WCM effectively omits the temporal evolution of the thermodynamic fields by computing them directly from the velocity field at each time step. In contrast, Oliva *et al.* (2025) found that the compressible work performed by the unsteady pressure field directly affects the energy of the fluid particles. Individual particles passing through vortical structures with associated unsteady pressure wells are therefore heated and cooled. The slip line between the high- and low speed flows, which constitutes a streamline, then acts as a boundary between the heated and cooled fluid entrained

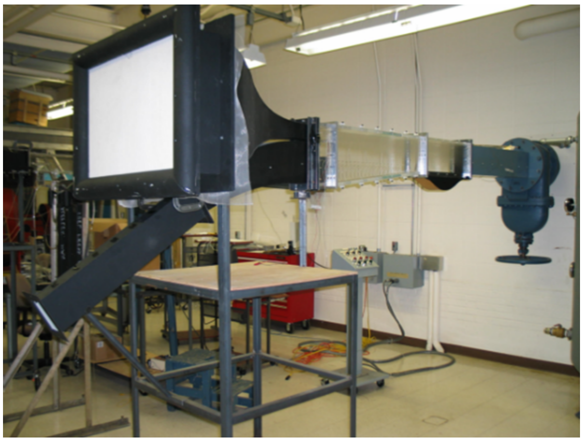

Figure 1: Compressible shear layer wind tunnel.

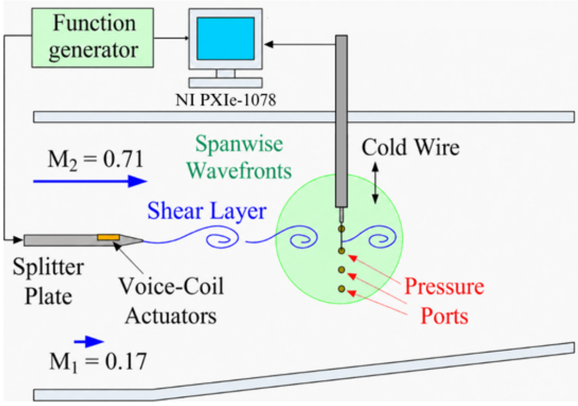

Figure 2: Schematic of the experimental setup.

by the vortical motion of the large-scale structures in the shear layer, producing sharp thermodynamic gradients. The omission of the thermodynamic history of individual fluid particles thus leads to artificially weak thermodynamic gradients.

The goal of the present study is to further investigate the existence of high magnitude stagnation temperature gradients through simultaneous calibrated cold-wire and wall-normal static pressure measurements of a subsonic compressible shear layer, in conjunction with digital holographic optical wavefront spanwise measurements that provide an approximation of the path integrated density field. This work provides the experimental basis for resolving existing ambiguities in the thermodynamic properties of the subsonic compressible shear layer, enabling future studies to better understand its fundamental behavior and the associated optical distortion mechanisms, and to develop better models to predict the optical distortions of the compressible shear layers.

Experimental Approach

Experimental measurements were conducted in the Compressible Shear Layer Wind Tunnel (CSLWT) at the University of Notre Dame, shown in Figure 1. The tunnel forms a shear layer using high and low speed inlets that produce a high speed flow with $M_2 \approx 0.71$ ($U_2 \approx 231$ m/s) and a low speed flow with $M_1 \approx 0.17$ ($U_1 \approx 57$ m/s). The combination of the two streams produces a weakly-compressible shear layer with a convective Mach number of $M_c \approx 0.26$, where the convective Mach number is defined as

$$M_{\text{conv}} = \frac{U_2 - U_1}{a_2 + a_1}, \tag{2}$$

with a denoting the speed of sound and subscripts 1 and 2 denoting the low- and high speed regions of the shear layer, respectively (Papamoschou & Roshko (1988)). Both inlets draw air from the same laboratory environment, ensuring a constant stagnation temperature between them. High pressure loss straw boxes are used to reduce the total pressure of the low speed flow, producing a constant static pressure across the two streams.

A splitter plate equipped with a voice coil actuator array at its trailing edge is used to provide flow excitation (Rennie *et al.* (2007)). This forcing controls the roll up of the shear layer, improving the spanwise uniformity of the resulting vortices, and regularizing the flow at the measurement location. Together, these effects increase the two-dimensionality of the flow and enable phase-locked measurements of static temperature, static pressure, and wavefront measurements. The frequency of the most unstable mode, f_e, and its subharmonic, $f_{e/2}$, were identified from the power spectral density of the forced shear layer using a set of candidate frequencies ranging from 650 to 1200 Hz. The shear layer responded most strongly at $f_e = 750$ Hz. Consequently, the shear layer in this study was forced at this frequency along with its subharmonic (375 Hz) at 10% of the fundamental amplitude to better control vortex formation and pairing at the measurement location (Duffin (2009)).

A schematic of the experimental article, indicating the temperature, pressure, and wavefront measurement locations within the CSLWT test section, are shown in Figure 2.

The experiment was designed such that all flow state measurements were centered on the same streamwise location, ≈ 0.28 m downstream of the splitter plate trailing edge. At this location, 13 Kulite XT-140-10D unsteady pressure transducers were arranged in a vertical (cross-stream) direction with a spacing of $\approx 1.3 \times 10^{-2}$ m; all sensors were mounted flush and wall-normal to the interior of the test section. Static temperature measurements were taken along a vertical line, using a cold-wire with Constant Current Anemometry (CCA). The locations of the temperature measurements were aligned with the unsteady pressure sensor array, at the centerline of the test section, displaced ≈ 0.05 m from the wall. A total of 11 cold-wire spatial points were obtained, vertically aligned with Kulite sensors 2–12. Both the unsteady pressure and cold-wire signals were recorded using a National Instruments PXIe-1078 DAQ system at a sampling rate of $f_s = 30{,}000$ Hz. Data acquisition was synchronized with the harmonic signal driving the voice coil actuators, ensuring that pressure and temperature data were acquired with a 0° phase offset relative to the peak of the voice coil signal. The cold-wire operating principle and calibration procedure are discussed in length in the following section.

A collimated laser beam with a diameter of ≈ 0.10 m was sent through the shear layer in the spanwise direction. The bean was centered on the unsteady pressure sensor array and used for wavefront measurements, using a high-speed off-axis digital holography wavefront sensor. Wavefront data were also recorded at $f_s = 30{,}000$ Hz, using a Phantom TMX-5010 high speed camera. Wavefront sensing is a non-intrusive measurement technique capable of resolving density fields along the path of a propagating beam through the Gladstone-Dale relation,

$$n = 1 + K_{GD}\rho. \tag{3}$$

Here, ρ denotes the density, n the index of refraction, and K_{GD} the Gladstone-Dale coefficient. The index of refraction, and consequently the density, can then be related to the optical wavefront of the analyzing beam through:

$$W(x,y,z,t) = -\int_0^L n'(x,y,z,t)\,\mathrm{d}z = -K_{GD}\int_0^L \rho(x,y,z,t)\,\mathrm{d}z. \tag{4}$$

For the purposes of this study, it is sufficient to note that the wavefront measurements provides a spanwise-integrated approximation of the density field at the measurement location,

$$\rho_L(x,y,t) = -\frac{1}{L}\int_0^L \rho_(x,y,z,t)\,\mathrm{d}z. \tag{5}$$

and are used here to verify the desired shear layer forcing and to identify vortex core locations. A complete description of the off axis digital holographic wavefront sensing technique can be found in Kipp *et al.* (2025).

Cold-Wire Operating Principle and Calibration

The operating principle of cold-wire CCA can be developed starting from the resistance of the wire, given by Bruun (1995) as

$$R_w = R_{w,0}\left[1+\alpha\left(T_w - T_{w,0}\right)\right]. \tag{6}$$

Here, R_w and T_w are the resistance and temperature of the wire, $R_{w,0}$ and $T_{w,0}$ are the resistance and temperature of the wire in a reference state, and α is the temperature coefficient of resistance. For temperature fluctuations about the mean, T'_w, Eq. 6 reduces to

$$R'_w = \alpha R_{w,0} T'_w. \tag{7}$$

By Ohm's law,

$$V' = I_w \alpha R_{w,0} T'_w, \tag{8}$$

where I_w is the constant current supplied to the cold-wire (5 mA in this study). Assuming negligible self heating, the wire temperature closely tracks the fluid temperature, $T'_f \approx T'_w$, yielding

$$T'_f \approx \frac{V'}{I_w \alpha R_{w,0}}. \tag{9}$$

Defining the sensitivity coefficient $S = I_w \alpha R_{w,0}$, S can be determined through thermal calibration of the cold-wire under quiescent conditions (Bruun (1995)). For this study, S was determined using a feedback controlled plenum in which the temperature was varied at regular intervals from 77.4°F to 180.0°F ($\approx$ 300-355 K). The resulting sensitivity for the present cold-wire was $S \approx 5.3\times10^{-6}$ V/K. With S known, the voltage fluctuations of the wire can be related to its recovery temperature as

$$T_r = \frac{V'}{S} + T_{ref}. \tag{10}$$

The static temperature can then be obtained from the recovery temperature via (Laurantzon *et al.* (2012))

$$T = \frac{T_r}{1 + r\dfrac{(\gamma-1)}{2}M^2}. \tag{11}$$

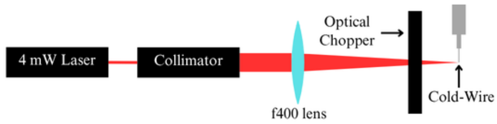

Figure 3: Experimental setup used to determine the time constant of the cold-wire CCA.

Here, the local Mach number M is taken from the velocity profile reported in Kipp *et al.* (2026), and the recovery factor is assumed to be $r = 0.84$ (Laurantzon *et al.* (2012)). Finally, the stagnation temperature follows from the static temperature through the isentropic relation

$$T_0 = T\left(1 + \frac{\gamma-1}{2}M^2\right). \tag{12}$$

In practice, however, the wire temperature fluctuations, T'_w, do not occur simultaneously with the fluid temperature fluctuations T'_f, as the thermal inertia of the wire causes its response to act as a first order low pass filter. To demonstrate that, we begin with the wire energy balance equation, also from Bruun (1995),

$$m_w c_w \frac{dT_w}{dt} = I_w^2 R_w - hA_w(T_w - T_f), \tag{13}$$

where m_w is the mass of the wire, c_w its specific heat capacity, and h the convective heat transfer coefficient. Because the wire current is intentionally small (5 mA), self heating is negligible, i.e. $I_w^2 R_w \approx 0$. Defining $q = hA_w(T_f - T_w)$ and perturbing q about a mean state gives

$$q' = A_w\left[h_0(T'_f - T'_w) + h'(T_{f,0} - T_{w,0})\right]. \tag{14}$$

In contrast to a hot-wire anemometry, the negligible self heating of the cold-wire ensures $T_{f,0} \approx T_{w,0}$, so the second term on the right hand side vanishes and $q' \approx A_w h_0(T'_f - T'_w)$. This minimizes the influence of velocity perturbations on the temperature of the wire, which would otherwise enter through $h'(T_{f,0} - T_{w,0})$ term (Lemay & Benaïssa (2001)). For the present operating conditions, velocity perturbations were estimated to contribute only 0.25-0.45 K ($<$ 4%) of the total wire temperature variation. Substituting the simplified form of Eq. 14 into Eq. 13 yields

$$m_w c_w \frac{dT'_w}{dt} = A_w h_0(T'_f - T'_w). \tag{15}$$

Defining the wire thermal time constant as $\tau_w = m_w c_w/(A_w h_0)$, the wire response can be expressed as the first order low pass system (Bruun (1995))

$$\tau_w \frac{dT'_w}{dt} + T'_w = T'_f, \tag{16}$$

with the associated transfer function

$$H(\omega) = \frac{1}{1 + j\omega\tau_w}, \qquad \hat{T}'_w(\omega) = H(\omega)\hat{T}'_f(\omega), \tag{17}$$

where the hat denotes Fourier Transformation. By experimentally determining the time constant, τ_w, this transfer function can be used to compensate for the amplitude attenuation

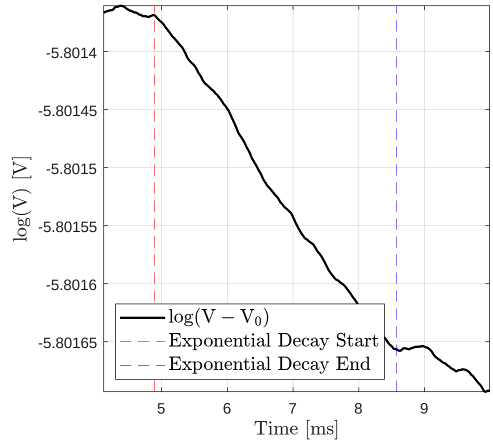

Figure 4: Log-linear decay region used to extract the cold-wire time constant.

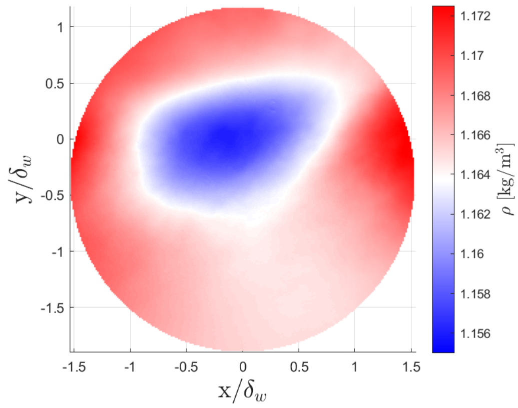

Figure 5: Phase averaged density field at $\phi = \pi/2$.

and the associated phase lag introduced by the thermal inertia of the cold wire and to recover the true fluid temperature fluctuations, T_f'. To calculate the transfer function, $H(\omega)$, the step response of the wire was measured using the setup shown in Figure 3. A 4 mW laser was brought to a focal point on the cold-wire surface using a beam expander/collimator and an $f = 400$ mm lens. Once aligned, an optical chopper was placed in the focused beam and configured to interrupt the beam at step-wise matter (light/no light) at the frequency of 100 Hz. By collecting the cold-wire CCA signal with the data acquisition setup described above, a representative step response could be constructed by block- and ensemble averaging the periodic signal, following an approach similar to that of Arwatz *et al.* (2013). The averaged signal was then examined to identify the expected log-linear decay region shown in Figure 4.

The portion of the signal between the annotated start and end of the exponential decay in Figure 4 was fit to the model

$$V(t) = Ae^{-t/\tau_w} + C \tag{18}$$

using the least squares regression. This procedure yielded a time constant of $\tau_w \approx 1.8$ ms. At $f_e = 750$ Hz, the resulting cold-wire transfer function attenuates the signal amplitude by $\approx 88\%$ and introduces a phase lag of $\approx 83°$. Knowing the time constant and using the transfer function, Eq. 17, the measured temperature fluctuations were subsequently corrected for in post processing via forward and inverse Fourier Transforms.

Results

This section presents the phase averaged results obtained from the calibrated test section. The number of frames per excitation period is given by the ratio, f_s/f_e, yielding a total of 40 frames per period. Figure 6 shows the phase averaged pressure data acquired by the unsteady pressure array. The wall-normal coordinate is normalized by the local vorticity thickness,

$$\delta_w = \frac{U_2 - U_1}{\left(\dfrac{\partial U}{\partial y}\right)_{\max}}, \tag{19}$$

with the velocity components taken from the velocity profile reported in Kipp *et al.* (2026). The shear layer centerline, denoted by $y/\delta_w = 0$ in Figure 6, was identified as the wall-normal location with the maximum peak to peak pressure fluctuations. The same centerline location was used in the temperature figures, while the wavefront centerline was determined analogously by locating the wall-normal position of maximum peak to peak density fluctuation.

Before discussing the results in detail, it is important to establish the frame of reference for the flow phenomena under consideration. In particular, defining what constitutes a vortex is essential when describing the particle motion that drives the proposed thermofluidic mechanisms. Following the definition adopted in DeFoor *et al.* (2026), a vortex is taken here as a low density core that entrains the surrounding fluid through vortical motion. To locate such a structure in phase space, we refer to Figure 5, which shows the phase averaged wavefront at a phase offset of $\pi/2$ converted into the corresponding density field via Eqs. 4 and 5.

A phase offset of $\phi = \pi/2$ corresponds to a centered vortex in the wavefront frame. Because the wavefront beam was centered on the unsteady pressure array and the streamwise location of the cold-wire probe, $\phi = \pi/2$ in the unsteady pressure and temperature measurements likewise corresponds to a centered vortex. For clarity, the phase position of the vortex is denoted $\phi_{\text{vortex}} = \pi/2$ in the discussion that follows.

When interpreting the phase averaged pressure and temperature fields, an important subtlety of phase averaging should be noted. For a flow structure traversing from left to right relative to the measurement location, structures that pass first appear on the rightmost edge of the phase averaged plot. The orientation of structures in phase space may therefore appear counterintuitive at first glance, therefore visualizing the structures mirrored about the vertical axis recovers a more natural streamwise depiction of the structure evolution.

Beginning with the pressure measurements, the location of the minimum of the static pressure field in Figure 6a can be compared to that of ϕ_{vortex}. As expected, the two coincide, reflecting the low density, low pressure cores associated with the shear layer vortical structures. An unexpected result is that the peak to peak fluctuations in static pressure correspond to only $\approx 1\%$ of the freestream static pressure value, providing pressure fluctuation magnitudes (and consequently $\partial P/\partial t$ magnitudes) approximately an order of magnitude smaller than those reported in DeFoor *et al.* (2026). The authors speculate that this discrepancy arises primarily from the combined effects of phase averaging and differences in f_e between the experimental and computational studies. To investigate, the pressure time series was examined directly to determine whether the phase wise instantaneous pressure gradient, $\partial P/\partial \phi$, agreed between the two datasets. Here, $\partial P/\partial \phi$ is defined as

$$\frac{\partial P}{\partial \phi} = \frac{1}{2\pi f_e}\frac{\partial P}{\partial t}. \tag{20}$$

Upon examining this form, the experimental and computational results agree well, with both exhibiting a peak to peak range of $\partial P/\partial \phi \approx 7000\,Pa/rad$. This indicates that the magnitude discrepancy in the phase averaged pressure fluctuations is consistent with the aforementioned averaging and forcing frequency effects rather than with a physical disagreement between the studies. For brevity, the figures associated with $\partial P/\partial \phi$ are omitted here but can be provided upon request to the corresponding author. The phase averaged unsteady pressure term, $\partial P/\partial t$, is shown in Figure 6b. By definition, $\partial P/\partial \phi$ leads the static pressure fluctuations by $\pi/2$. More importantly, at ϕ_{vortex}, a positive $\partial P/\partial t$ well leads the vortex and a negative $\partial P/\partial t$ well trails it.

The phase-locked static temperature fields, shown in Figure 7, exhibit the structures expected for the phase-locked vortex at ϕ_{vortex}. The shape of the perturbed slip line separating the high- and low static temperature regions in Figure 7a is consistent with the speed differential between the two streams forming the shear layer. The stagnation temperature field in Figure 7b reveals two vertically offset, co-rotating stagnation temperature lobes. Their existence alone is sufficient to demonstrate that the WCM does not capture the relevant thermodynamics of a shear layer in this regime. Furthermore, the presence of high magnitude stagnation temperature gradients between the lobes reinforces this conclusion, since such gradients were argued in Fitzgerald & Jumper (2004) to be physically inadmissible within the WCM framework.

The mechanism producing these stagnation temperature lobes, as proposed in DeFoor *et al.* (2026), results from the combined action of the vortical motion at the vortex location, ϕ_{vortex}, and the relative positioning of the positive-negative $\partial P/\partial t$ regions. Specifically, according to Eq. 1, unsteady pressure related work performed on fluid particles as they traverse the regions of positive $\partial P/\partial t$ under the influence of vortical motion increases their total energy (T_0). After passing the center of the vortical structure, the continuing vortical motion transports these now energized particles into a region with negative $\partial P/\partial t$ values. The net result is the formation of co-rotating total temperature lobes which lag approximately $\pi/2$ radians behind the unsteady pressure wells, as seen by comparing Figures 6b and 7b.

CONCLUSION

This study presented simultaneous, phase averaged experimental measurements of static pressure, static and stagnation temperature, and inferred density fields of a forced subsonic compressible shear layer at a convective Mach number of $M_c \approx 0.26$. Static pressure was measured directly with a wall-normal array of unsteady pressure sensors. Static temperature fields were obtained from calibrated cold-wire Constant Current Anemometry corrected for effects of thermal inertia of the wire using the first order model. Additional experiments were conducted to investigate the step response of the cold-wire CCA were conducted, and the time constant of the response was calculated. Off-axis digital holographic wavefront measurements provided estimates of the spanwise-averaged density field, used to both confirm successful shear layer forcing and supply a phase reference to identify the shear layer vortical structure.

Three main observations were made from this experimental study. First, the static pressure minima, associated with a pressure well inside the vortical structure, coincide in phase with the low density vortex cores identified from the wavefront- derived density field, while the unsteady pressure term, $\partial P/\partial t$, exhibits a leading positive region and a trailing negative region aligned with the vortex. Second, although the absolute magnitudes of the phase averaged static pressure fluctuations are roughly an order of magnitude smaller than those reported in the companion CFD study of DeFoor *et al.* (2026), the phase-locked pressure gradient, $\partial P/\partial \phi$, which removes the dependence on forcing frequency, agrees between the two studies to within the experimental uncertainty. Third, the measured stagnation temperature field exhibits two vertically offset, co-rotating lobes separated by sharp gradients, and these lobes lag approximately $\pi/2$ radians behind the maxima of the unsteady pressure wells, associated with the vortex.

Taken together, these results constitute direct experimental evidence that the Weakly Compressible Model is not, on its own, sufficient to describe the thermodynamic behavior of a shear layer in this regime, since it does not predict the sharp stagnation temperature gradients or the offset, co-rotating lobe structure observed in the experiment. In contrast, the measurements are consistent with the thermo-fluidic mechanism proposed upon performing numerical simulations of the shear layer in DeFoor *et al.* (2026); Oliva *et al.* (2025). The presented studies confirm that compressible work performed by the unsteady pressure field on fluid particles transported by vortical motion accumulates along particle pathlines, with the slip line acting as a boundary that separates regions of heated and cooled entrained fluid.

Future work will utilize additional optical flow diagnostic techniques with improved spanwise resolution such as a Focusing Schlieren approach. This approach will allow more direct comparison of the predicted two-dimensional planes of the density field from complementary simulations with the experimental data. Moreover, an analog circuit is currently under development to provide a direct frequency compensation of the CCA performance without the need for post-process compensation and additional studies into the thermal inertia of the cold-wire. In conjunction with these improvements, the ultimate goal of the authors is to combine computational and experimental efforts to further investigate the thermo-fluidic mechanisms of the transonic shear layer, and to use the results to improve modeling tools to predict optical performance of the weakly-compressible shear layers.

REFERENCES

Arwatz, Gilad, Bahri, Carla, Smits, Alexander J & Hultmark, Marcus 2013 Dynamic calibration and modeling of a cold wire for temperature measurement. *Measurement Science and Technology* **24** (12), 125301.

Bruun, H H 1995 *Hot-Wire Anemometry: Principles and Signal Analysis*. Oxford University Press.

DeFoor, Thomas E., Oliva, Andrew A. & Rennie, Mark R. 2026 Computational Investigation of the Thermo-Fluid Mechanisms for Aero-Optical Distortions in a Subsonic Compressible Shear Layer. In *AIAA SCITECH 2026 Forum*. American Institute of Aeronautics and Astronautics, _eprint: https://arc.aiaa.org/doi/pdf/10.2514/6.2026-1150.

Duffin, Daniel Anthony 2009 Feed-Forward Adaptive-Optic Correction of a Weakly-Compressible High-Subsonic Shear Layer. thesis, University of Notre Dame.

Fitzgerald, E. J. & Jumper, E. J. 2004 The optical distortion mechanism in a nearly incompressible free shear layer. *Journal of Fluid Mechanics* **512**, 153–189.

Gordeyev, S., Jumper, E.J. & Whiteley, M.R. 2023 *Aero-*

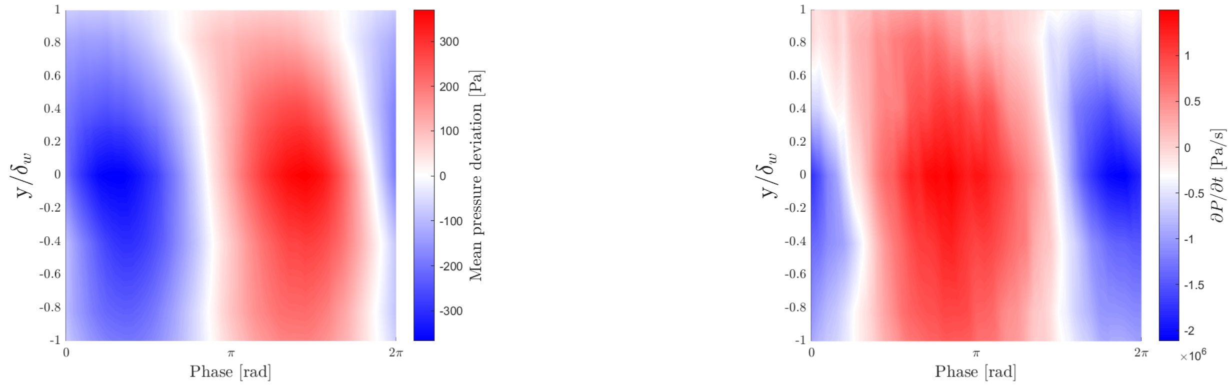

(a) Phase averaged static pressure, P, field.

(b) Phase averaged $\partial P/\partial t$ field.

Figure 6: Phase averaged pressure data.

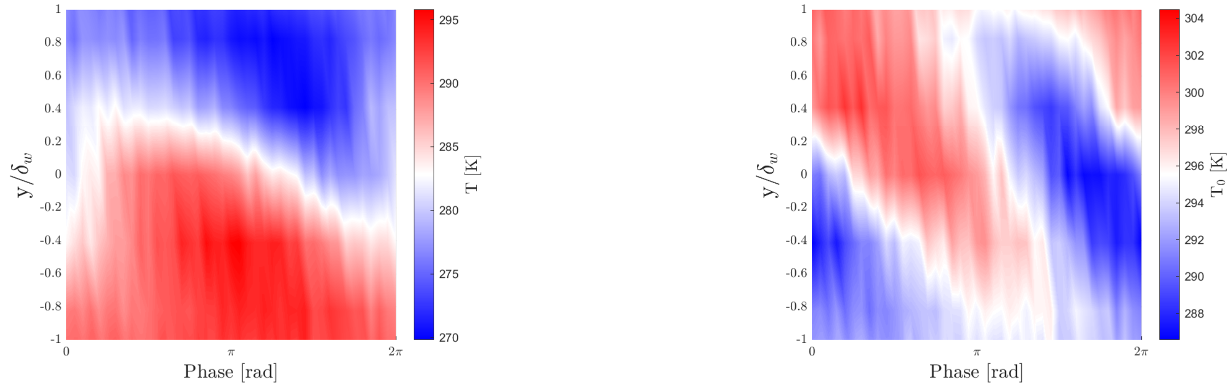

(a) Phase averaged static temperature, T, field.

(b) Phase averaged total temperature, T_0, field.

Figure 7: Phase averaged temperature data.

Optical Effects: Physics, Analysis and Mitigation, 1st edn. John Wiley & Sons.

Kipp, Carson, Bukowski, Timothy, Rennie, Robert & Gordeyev, Stanislav 2026 Comparison of Shack–Hartmann and digital holographic measurements of the optical effect of a subsonic compressible shear layer. *Optical Engineering* **65**.

Kipp, C. M., Bukowski, T.J., Rennie, R.M. & Gordeyev, S. 2025 Simultaneous shack-hartmann and digital holography measurements of the optical effect of a subsonic compressible shear layer. In *Unconventional Imaging, Sensing, and Adaptive Optics 2025*, , vol. 13619, p. 136190P.

Laurantzon, Fredrik, Tillmark, Nils & Alfredsson, P. Henrik 2012 What does the hot-wire measure? *Proceedings of the 16th International Symposium on Applications of Laser Techniques to Fluid Mechanics* .

Lemay, J. & Benaïssa, A. 2001 Improvement of cold-wire response for measurement of temperature dissipation. *Experiments in Fluids* **31** (3), 347–356.

Oliva, A.A., DeFoor, T.E. & Rennie, R.M. 2025 Computational investigation of aero-optical discrepancies in a free shear layer. In *Unconventional Imaging, Sensing, and Adaptive Optics 2025*, , vol. 13619, p. 136190N.

Papamoschou, Dimitri & Roshko, Anatol 1988 The compressible turbulent shear layer: an experimental study. *Journal of Fluid Mechanics* **197**, 453–477.

Rennie, M., Duffin, D. & Jumper, E. 2007 Characterization of a Forced Two-Dimensional, Weakly-Compressible Shear Layer. In *38th Plasmadynamics and Lasers Conference*. AIAA Paper 2007-4007.

Rennie, M., Ponder, Z., Gordeyev, S., Nightingale, A. & Jumper, E. 2008 Numerical investigation of two-dimensional compressible shear layer and comparison to weakly compressible model. In *Directed Energy Professional Society, Beam Control Conference, Monterey, CA, 3-7 March 2008*.

Visbal, M. 2009 Numerical simulation of aero-optical aberration through a weakly compressible shear layer. In *39th AIAA Fluid Dynamics Conference*. AIAA Paper 2009-4298.